Wavelet methods for shape perception in electro-sensing

Irène Waldspurger, Habib Ammari, Stéphane Mallat, Han Wang

Wavelet methods for shape perception in electro-sensing *

Habib Ammari†, Stéphane Mallat‡, Irène Waldspurger‡, and Han Wang†

October 11, 2013

Abstract

This paper aims at presenting a new approach to the electro-sensing problem using wavelets. It provides an efficient algorithm for recognizing the shape of a target from micro-electrical impedance measurements. Stability and resolution capabilities of the proposed algorithm are quantified in numerical simulations.

Mathematics Subject Classification (MSC2000): 35R30, 35B30

Keywords: electro-sensing, classification, recognition, shape descriptors, wavelets

1 Introduction

The aim of electro-sensing is to learn geometric parameters and material compositions of a target via electrical measurements. In this paper, we suppose that the target is composed of a homogeneous material with a known electrical property and focus uniquely on the problem of geometry. Geometric identification of a target may mean to recognize it from a collection of known shapes (up to rigid transformations and scaling), or to reconstruct its boundary.

In the recent work [2], an approach based on polynomial basis has been proposed for the far-field measurement system. Using Taylor expansion of the Green functions, on one hand, the geometric information of the target can be coded in some features, which are the action of a boundary integral operator on homogeneous polynomials of different orders, and on the other hand the measurement system is separated into a linear operator relating the features to the data. The features are then extracted by solving a linear inverse problem and can be used to identify the target in a database. Unlike other methods (*e.g.* in electrical impedance tomography [9]) which attempt to reconstruct directly the target, this approach is more effective and computationally efficient in the applications of shape recognition.

From a more general point of view, the problem is to know, given the physical configuration of the measurement system, how to choose the basis for representation of features

*This work was supported by ERC Advanced Grant Project MULTIMOD–267184.

†Department of Mathematics and Applications, Ecole Normale Supérieure, 45 Rue d'Ulm, 75005 Paris, France (ammari@dma.ens.fr, wang@dma.ens.fr).

‡Computer Science Department, Ecole Normale Supérieure, 45 Rue d'Ulm, 75005 Paris, France (mallat@di.ens.fr, waldspur@di.ens.fr).

and how to extract them from data for identification. The ill-posedness in electro-sensing is inherent to the diffusion character of the currents and cannot be removed by a change of basis. Nonetheless, the particularity of a basis can modify totally the way in which information is organized in the feature and the manner in which it should be reconstructed.

In this paper we present a new approach for electro-sensing with the near-field measurement system using the wavelet basis. Unlike the far-field measurement configuration which is known to be exponentially unstable, the near-field measurement system is much more stable and the data reside in a higher dimensional subspace, hence one can expect to reconstruct more information of the target from the data. With the near-field measurement system, the new approach based on wavelet presents more advantages than the approach based on polynomials, for the reason that the wavelet representation of the features is local and sparse, and reflects directly the geometric character of a target. Furthermore, the features can be effectively reconstructed by seeking a sparse solution via ℓ^1 minimization, and the boundary of the target can be read off from the features, giving a new high resolution imaging algorithm which is robust to noise.

This paper is organized as follows. In section 2 we give a mathematical formulation and present an abstract framework for electro-sensing. We introduce the basis of representation and deduce a linear system by separating the features from the measurement system. The question of the stability of the measurement system is discussed. In section 3 we summarize essential results based on polynomial basis developed in [2]. The wavelet basis and new imaging algorithms, which are the main contributions of this paper, are presented in section 4, where we discuss some important properties of the wavelet representation and formulate the ℓ^1 minimization problem for the reconstruction of the features. Numerical results are given in section 5, and followed by some discussions in section 6. The paper ends with some concluding remarks.

2 Modelling of the electro-sensing problem

Let $D \subset \mathbb{R}^2$ be an open bounded domain of $\mathcal{C}^2$-boundary that we want to characterize via electro-sensing. We suppose that D is centered around the origin and has size 1, furthermore there exists $\Omega \subset [-1,1]^2$ an *a priori* open bounded domain such that D is compactly contained in the convex envelope of Ω (in practice, both the center of D and Ω can be estimated using some *location search algorithm* [5, 17]). We also assume that the positive conductivity number $\kappa \neq 1$ of D is known, and the background conductivity is 1. We denote by $D^c = \mathbb{R}^2 \setminus \overline{D}$.

A measurement system consists of N_s sources $\{x_s\}_{s=1\ldots N_s}$, and N_r receivers $\{y_r\}_{r=1\ldots N_r}$ disposed on Ω. The potential field u_s generated by the point source x_s is the solution to the equation

$$\begin{cases} \nabla.((1+(\kappa-1)\chi_D)\nabla u_s) = \delta_{x_s} \quad \text{in } \mathbb{R}^2, \\ u_s - \Gamma_s = O(|x|^{-1}) \quad \text{as } |x| \to \infty, \end{cases} \tag{1}$$

where χ_D is the indicator function of D, and $\Gamma_s(x) := \Gamma(x - x_s) = \frac{1}{2\pi}\log|x - x_s|$ is the background potential field. Similarly, we denote $\Gamma_r(x) := \Gamma(x - y_r)$.

The difference $u_s - \Gamma_s$ is the perturbation of potential field due to the presence of D in

the background, and evaluated at the receiver y_r it gives the measurement

$$V_{sr} = u_s(y_r) - \Gamma_s(y_r), \tag{2}$$

which builds the multistatic response matrix $\mathbf{V} = (V_{sr})_{sr}$ by varying the source and receiver pair. In this section, we show that with the help of a bilinear form, the problem can be formulated through a linear system relating the data $\mathbf{V}$ and the features of D.

2.1 Layer potentials and representation of the solution

Recall the single layer potential $\mathcal{S}_D$:

$$\mathcal{S}_D\left[\phi\right](x) = \int_{\partial D} \Gamma(x-y)\phi(y)ds(y), \tag{3}$$

and the *Neumann-Poincaré* operator $\mathcal{K}_D^*$:

$$\mathcal{K}_D^*\left[\phi\right](x) = \frac{1}{2\pi}\int_{\partial D} \frac{\langle x-y, \nu_x\rangle}{|x-y|^2}\phi(y)ds(y), \tag{4}$$

where ν_x is the outward normal vector at $x \in \partial D$. $\mathcal{K}_D^*$ is a compact operator on $L^2(\partial D)$ for a $\mathcal{C}^2$ domain D and has a discrete spectrum in the interval $(-1/2, 1/2]$. Therefore, the operator $(\lambda I - \mathcal{K}_D^*)$ is invertible on $L^2(\partial D)$ for the constant

$$\lambda = \frac{\kappa+1}{2(\kappa-1)}. \tag{5}$$

Moreover, its inverse $(\lambda I - \mathcal{K}_D^*)^{-1} : L^2(\partial D) \to L^2(\partial D)$ is also bounded. An important relation is the jump formula:

$$\frac{\partial \mathcal{S}_D\left[\phi\right]}{\partial \nu}\Big|_{\pm} = \left(\pm\frac{1}{2}I + \mathcal{K}_D^*\right)[\phi], \tag{6}$$

where $\partial/\partial\nu$ denotes the normal derivative across the boundary ∂D and $\pm$ indicate the limits of a function from outside and inside of the boundary, respectively. Details on these operators can be found in [7].

With the help of these operators, the solution u_s of (1) can be represented as

$$u_s(x) = \Gamma_s(x) + \mathcal{S}_D\left[\phi\right](x) \tag{7}$$

with ϕ satisfying $(\lambda I - \mathcal{K}_D^*)\left[\phi\right] = \partial\Gamma_s/\partial\nu$ on ∂D. Therefore, the perturbed field can be expressed as

$$(u_s - \Gamma_s)(x) = \int_{\partial D} \Gamma(x-y)(\lambda I - \mathcal{K}_D^*)^{-1}\left[\frac{\partial \Gamma_s}{\partial \nu}\right](y)ds(y). \tag{8}$$

We assume in the sequel $x_s, y_r \notin \partial D$ for all s, r which is necessary for V_{sr} to be well defined.

2.2 Bilinear form $\mathcal{T}$

We denote by $H^s(\Omega)$, for $s = 1, 2$, the standard Sobolev spaces and introduce the bilinear form $\mathcal{T} : H^2(\Omega) \times H^1(\Omega) \to \mathbb{R}$ defined as follows

$$\mathcal{T}(f, g) := \int_{\partial D} g(x)(\lambda I - \mathcal{K}_D^*)^{-1} \left[\frac{\partial f}{\partial \nu}\right](x)\, ds(x) \quad \text{for } f \in H^2(\Omega), g \in H^1(\Omega). \tag{9}$$

By the boundeness of $(\lambda I - \mathcal{K}_D^*)^{-1}$ and of the trace operator, it follows that

$$|\mathcal{T}(f, g)| \leq C\|f\|_{H^2}\|g\|_{H^1},$$

and hence, $\mathcal{T}$ is bounded. Now, we observe from (2) and (8) that V_{sr} can be rewritten as

$$V_{sr} = \mathcal{T}(\Gamma_s, \Gamma_r). \tag{10}$$

2.2.1 Characterization of D by $\mathcal{T}$

One of the interests of $\mathcal{T}$ is that it determines uniquely the domain D, as stated in the following result.

Proposition 2.1. *Let $D, D' \subset \Omega$ be open bounded domains with $\mathcal{C}^2$-boundaries with the same conductivity $\kappa \neq 1$, then $D = D'$ if and only if their associated bilinear forms are equal:*

$$\mathcal{T}_D(f, g) = \mathcal{T}_{D'}(f, g)\ \forall f \in H^2(\Omega), g \in H^1(\Omega). \tag{11}$$

Proof. Clearly $D = D'$ implies that $\mathcal{T}_D = \mathcal{T}_{D'}$. Now suppose $D \neq D'$. There exist a point $x \in \partial D \setminus \partial D'$. Let $\mathcal{V}$ be a small open neighborhood of x such that $\mathcal{V} \cap \partial D' = \emptyset$.

Let $f \in \mathcal{C}_0^\infty(\Omega)$ verifying that the support of f is included in $\mathcal{V}$ and $\frac{\partial f}{\partial \nu} \not\equiv 0$ over $\mathcal{V} \cap \partial D$. Such a f can be constructed for example in the following way. Let φ be a compactly supported $\mathcal{C}^\infty$ function, whose support is included in $\mathcal{V}$ and $\phi = 1$ in a small neighborhood of x. Then the function

$$f : y \mapsto \varphi(y)\langle y, \nu_x\rangle$$

satisfies the required conditions: its support is included in $\mathcal{V}$ and $\frac{\partial f}{\partial \nu}(x) = 1$ (in a neighborhood of x, f coincides with the function $y \mapsto \langle y, \nu_x\rangle$, whose gradient is ν_x).

We set $h = (\lambda I - \mathcal{K}_D^*)^{-1}\left[\frac{\partial f}{\partial \nu}\right] \in L^2(\partial D)$, which is not identically zero because $(\lambda I - \mathcal{K}_D^*)[h] = \frac{\partial f}{\partial \nu}$. Consequently, by the density of the image of the trace operator in $L^2(\partial D)$, there exist $g \in \mathcal{C}^\infty(\Omega)$ such that

$$\mathcal{T}(f, g) = \int_{\partial D} g(x)h(x)ds(x) \neq 0.$$

On the other hand, $(\lambda I - \mathcal{K}_{D'}^*)\left[\frac{\partial f}{\partial \nu}\right] = 0$ over $\partial D'$ because $\frac{\partial f}{\partial \nu} = 0$ over $\partial D'$. So $\mathcal{T}_{D'}(f, g) = 0$, which implies $\mathcal{T}_D \neq \mathcal{T}_{D'}$. □

2.3 Representation of $\mathcal{T}$

As suggested by Proposition 2.1, all information about D is contained in $\mathcal{T}$. This motivates us to represent $\mathcal{T}$ in a discrete form (features of D) that will be estimated from the data.

2.3.1 Basis of representation

Let $\mathcal{B} = \{e_n \in L^2(\Omega)\}_{n\in\mathbb{N}}$ be a Schauder basis of $L^2(\Omega)$. We denote by V_K the finite dimensional subspace spanned by $\{e_n\}_{n\leq K}$ and P_K the orthogonal projector onto V_K:

$$P_K f = \inf_{g\in V_K} \|f - g\|_{L^2(\Omega)}. \tag{12}$$

We require the following conditions on the basis $\mathcal{B}$:

- For any $f \in H^s(\Omega), s = 1, 2,$

$$\|f - P_K f\|_{H^s(\Omega)} \to 0 \quad \text{as } K \to +\infty. \tag{13}$$

- There exists a function $u(s,t)$ such that for $s = 1, 2$ and some $t > s$, we have $u(s,t) > 0$. Furthermore, it holds for any $f \in H^t(\Omega)$

$$\|f - P_K f\|_{H^s(\Omega)} \leq C K^{-u(s,t)} \|f\|_{H^t(\Omega)} \quad \text{as } K \to +\infty \tag{14}$$

  with the constant C being independent of K and f.

2.3.2 Polynomial basis

The first example of $\mathcal{B}$ is the homogeneous polynomial basis. The property (13) is a direct consequence of the following classical result (see Appendix A for its proof):

Lemma 2.2. *Let $|\alpha|_\infty := \max_i \alpha_i$. The family of polynomials $\{x^\alpha, |\alpha|_\infty \leq K\}_{K\geq 0}$ is complete in $H^s(\Omega)$ for $s \geq 0$.*

Estimate (14) can be obtained using an equivalent result of Legendre polynomials established in [11], with $u(s,t) = t - 2s + 1/2$.

2.3.3 Wavelet basis

Another example of $\mathcal{B}$ is the wavelet basis. Let $\tilde{\phi} \in \mathcal{C}_0^r(\mathbb{R}), r \geq 2$ be a one-dimensional orthonormal scaling function generating a multi-resolution analysis [19], and let $\tilde{\psi} \in L^2(\mathbb{R})$ be a wavelet which is orthogonal to $\tilde{\phi}$ and has $p > 2$ zero moments. We construct the two-dimensional scaling function $\phi = \psi^0$ by tensor product as $\phi(x_1, x_2) = \tilde{\phi}(x_1)\tilde{\phi}(x_2)$, and similarly we construct the wavelets ψ^k for $k = 1, 2, 3$ by tensor product of $\tilde{\phi}, \tilde{\psi}$ [19]. We denote by

$$\psi^k_{j,n}(x) := 2^{-j}\psi^k(2^{-j}x - n), \ j \in \mathbb{Z}, n \in \mathbb{Z}^2.$$

Then $\{\psi^k_{j,n}\}_{k,j,n}$ for $j \in \mathbb{Z}, n \in \mathbb{Z}^2, k = 1, 2, 3$, constitute an orthonormal basis of $L^2(\mathbb{R}^2)$. Particularly, the Daubechies wavelet of order 6 (with 6 zero moments) fulfills the conditions above [15].

Let V_j be the approximation space spanned by $\{\phi_{j,n}\}_{n\in\mathbb{Z}^2}$, and P_j be the orthogonal projector onto V_j:

$$P_j f = \sum_{n\in\mathbb{Z}^2} \langle f, \phi_{j,n}\rangle \phi_{j,n}. \tag{15}$$

The property (13) follows from the fact that the $P_j f$ converges to f in $H^s(\Omega)$ for any $|s| \leq r$ (see [21, Theorem 6, Chapter 2]).

The wavelet basis introduced above verifies the polynomial exactness of order $p-1$ [19] (*i.e.*, the polynomials of order $p-1$ belong to V_0) and $\phi \in H^s(\mathbb{R}^2)$ for $s = 1, 2$. Therefore, we have the following result (see [14, Corollary 3.4.1]): For any $f \in H^t(\Omega), s < t \leq p$

$$\|P_j f - f\|_{H^s(\Omega)} \lesssim 2^{j(t-s)} \|f\|_{H^t(\Omega)} \quad \text{as } j \to -\infty. \tag{16}$$

Then the estimate (14) is fulfilled with $u(s,t) = (t-s)/2$. By abuse of notation, throughout this paper, we still use P_K (with $K \propto 2^{-2j}$) to denote the projection for the wavelet basis.

2.3.4 Truncation of $\mathcal{T}$

Thanks to the boundedness of $\mathcal{T}$ and property (13), one can verify easily that for any $f \in H^2(\Omega), g \in H^1(\Omega)$

$$\mathcal{T}(f,g) = \mathcal{T}(P_K f, P_K g) + o(1), \tag{17}$$

with the truncation error $o(1)$ decaying to zero as $K \to +\infty$. Using the approximation property (14), a bound on the truncation error $o(1)$ can be established.

Proposition 2.3. *Suppose that the basis $\mathcal{B}$ fulfills the conditions (13) and (14). Let $\tilde{u}(t,t') := \min(u(2,t), u(1,t'))$ with the constants $t > 2$ and $t' > 1$ being those of estimate (14). Then for any $f \in H^t(\Omega), g \in H^{t'}(\Omega)$*

$$|\mathcal{T}(P_K f, P_K g) - \mathcal{T}(f,g)| \leq C K^{-\tilde{u}(t,t')} \quad \text{as } K \to +\infty, \tag{18}$$

where the constant C depends only on f, g, t, and t'.

Proof. By the triangle inequality

$$|\mathcal{T}(P_K f, P_K g) - \mathcal{T}(f,g)| \leq |\mathcal{T}(P_K f - f, P_K g)| + |\mathcal{T}(f, P_K g - g)|. \tag{19}$$

Using the boundedness of $\mathcal{T}$ on the first term of the right-hand side, we get

$$|\mathcal{T}(P_K f - f, P_K g)| \leq C \|P_K f - f\|_{H^2} \|P_K g\|_{H^1}.$$

On one hand, one can apply (14) on $\|P_K f - f\|_{H^2}$ with the constant $t > 2$ verifying $u(2,t) > 0$. On the other hand, for any $t' > 1$ and $g \in H^{t'}(\Omega)$ we have $P_K g \to g$ in $H^1(\Omega)$ by (13). Therefore, we obtain that

$$|\mathcal{T}(P_K f - f, P_K g)| \lesssim K^{-u(2,t)} \|f\|_{H^t} \|g\|_{H^1}.$$

Similarly, for the second term of the right-hand side in (19) we get

$$|\mathcal{T}(f, P_K g - g)| \leq C \|f\|_{H^2} \|P_K g - g\|_{H^1} \lesssim K^{-u(1,t')} \|f\|_{H^2} \|g\|_{H^{t'}},$$

which holds for any $g \in H^{t'}(\Omega)$ for the constant $t' > 1$ of (14). Combining these two terms yields the desired result. □

2.3.5 Coefficient matrix

We define the coefficient matrix $\mathbf{X}$ as follows

$$\mathbf{X} = \mathbf{X}[D, K] = (\mathcal{T}(e_m, e_n))_{mn} \quad \text{for } m, n = 1 \dots K, \tag{20}$$

which represents $\mathcal{T}$ under the basis $\mathcal{B}$ up to the order K. We denote by $\mathbf{f}$ the coefficient vector of $P_K f$, *i.e.*,

$$P_K f = \sum_{n \le K} \mathbf{f}_n e_n, \tag{21}$$

and similarly $\mathbf{g}$ for $P_K g$. Then $\mathcal{T}$ restricted on V_K can be put into the following matrix form:

$$\mathcal{T}(P_K f, P_K g) = \sum_{m,n=1}^{K} \mathbf{f}_m \mathcal{T}(e_m, e_n) \mathbf{g}_n = \mathbf{f}^\top \mathbf{X} \mathbf{g}. \tag{22}$$

Thanks to property (13) of the basis, there is a one-to-one mapping between $\mathcal{T}$ and its coefficient matrix $\mathbf{X}$ as $K \to +\infty$. Hence the domain D is also uniquely determined from $\mathbf{X}[D]$ when $K \to +\infty$, as a consequence of Proposition 2.1.

2.4 Linear system

In (10), the Green functions Γ_s and Γ_r play the role of the measurement system while the information about D is contained in the operator $\mathcal{T}$. This motivates us to separate these two parts and extract information about D from the data $\mathbf{V}$.

By removing a small neighborhood of x_s and y_r if necessary, we can always assume that Ω does not contain any source or receiver, in such a way that Γ_s and Γ_r restricted on Ω become $\mathcal{C}^\infty$, and hence can be represented using the basis $\mathcal{B}$ (note that since $x_s, y_r \notin \partial D$, removing the singularity does not affect $\mathcal{T}(\Gamma_s, \Gamma_r)$ which depends only on the value of the Green functions on ∂D).

We denote in the sequel $\boldsymbol{\gamma}_{x_s}, \boldsymbol{\gamma}_{y_r} \in \mathbb{R}^K$ the (column) coefficient vectors of $P_K \Gamma_s$ and $P_K \Gamma_r$, respectively. From (10), (17) and (22) one can write

$$V_{sr} = \mathcal{T}(\Gamma_s, \Gamma_r) = {\boldsymbol{\gamma}_{x_s}}^\top \mathbf{X} \boldsymbol{\gamma}_{y_r} + E_{sr} \tag{23}$$

with E_{sr} being the truncation error of order K which can be controlled using Proposition 2.3. We introduce the matrices of the measurement system

$$\boldsymbol{\Gamma}_\mathbf{s} = [\boldsymbol{\gamma}_{x_1} \dots \boldsymbol{\gamma}_{x_{N_s}}], \quad \boldsymbol{\Gamma}_\mathbf{r} = [\boldsymbol{\gamma}_{y_1} \dots \boldsymbol{\gamma}_{y_{N_r}}], \tag{24}$$

as well as the linear operator $\mathbf{L} : \mathbb{R}^{K \times K} \to \mathbb{R}^{N_s \times N_r}$:

$$\mathbf{L}(\mathbf{X}) = {\boldsymbol{\Gamma}_\mathbf{s}}^\top \mathbf{X} \boldsymbol{\Gamma}_\mathbf{r}. \tag{25}$$

Then (23) can be put into a matrix product form:

$$\mathbf{V} = {\boldsymbol{\Gamma}_\mathbf{s}}^\top \mathbf{X} \boldsymbol{\Gamma}_\mathbf{r} + \mathbf{E} = \mathbf{L}(\mathbf{X}) + \mathbf{E} \tag{26}$$

with $\mathbf{E} = (E_{sr})_{sr}$ being the matrix of truncation error. Further, suppose that $\mathbf{V}$ is contaminated by some measurement noise $\mathbf{N}_{\text{noise}}$, *i.e.*, the m,n-th coefficient follows the normal distribution

$$(\mathbf{N}_{\text{noise}})_{mn} \overset{\text{iid}}{\sim} \mathcal{N}(0, \sigma_{\text{noise}})$$

with $\sigma_{\text{noise}} > 0$ being the noise level. Using the bound (18) of the truncation error, we can assume that for a large K

$$|E_{sr}| \ll \sigma_{\text{noise}} \tag{27}$$

uniformly in all s and r, so that $\mathbf{E}$ can be neglected compared to the noise. Finally, we obtain a linear system relating the coefficient matrix to the data

$$\mathbf{V} = \mathbf{L}(\mathbf{X}) + \mathbf{N}_{\text{noise}}, \tag{28}$$

and the objective is then to estimate $\mathbf{X}$ from $\mathbf{V}$ by solving (28).

2.4.1 Measurement systems and stability

The stability of the operator $\mathbf{L}$ is inherent to the spatial distribution of sources and receivers that we suppose to be coincident in what follows. The far-field measurement system (Figure 1 (a)) is the situation when the characteristic distance ρ between transmitters and the boundary of the target is much larger than the size δ of the target. On the contrary, in the near-field internal measurement system (Figure 1 (b)) which is used in micro-EIT [18, 20], we have $\rho \ll \delta$ and the transmitters can be placed "inside" the target. Other types of far-field measurements exist; see [1, 4].

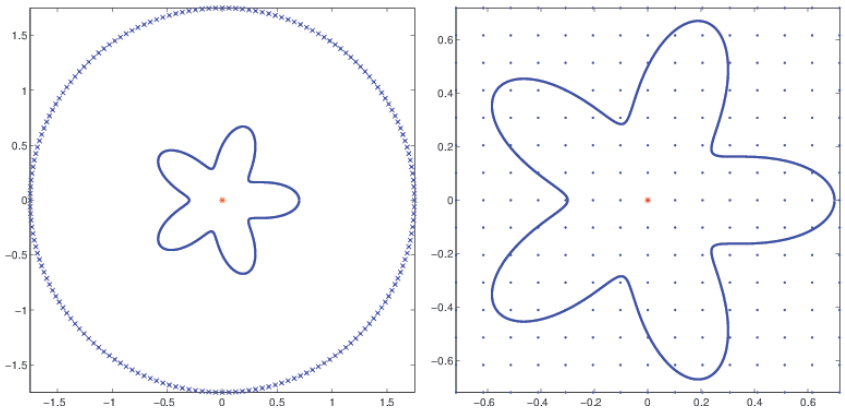

(a) Far-field measurement (b) Near-field measurement

Figure 1: Far-field and near-field measurement systems with a flower-shaped target D. (a): 360 coincided sources and receivers (cross) are uniformly distributed on a circle including the target. (b): 15× 15 coincided sources and receivers (dots) are uniformly distributed inside Ω, and the minimal distance to ∂D is $\sim 10^{-3}$. The red cross in both figures marks the center of Ω.

Note that a singular value of $\mathbf{L}$ is the product of a pair of singular values of $\mathbf{\Gamma_s}$ and $\mathbf{\Gamma_r}$. In Figure 2 we compare the distribution of the singular values of the operator $\mathbf{L}$ (computed with the Daubechies wavelet of order 6 as $\mathcal{B}$) corresponding to the systems of Figure 1. One can notice the substantial difference between these two systems: the singular values of the far-field system decays very fast, revealing the exponential ill-posedness of the associated inverse problem [2, 3, 6]. On the contrary, for the near-field system, the stability of $\mathbf{L}$ is considerably improved. This can be explained by the decay of the wavelet coefficients of the Green function. In fact, Γ_s is smooth away from x_s, therefore most rows (populated by detail wavelet coefficients) in $\mathbf{\Gamma_s}$ have tiny numerical values which make the matrix ill-conditioned. More precisely, the following result holds. We refer to Appendix B) for its proof.

Proposition 2.4. *Let F be a compact domain. Suppose that $x_s \notin F$ and denote by ρ the distance between x_s and F. If the wavelet $\psi^k, k = 1, 2, 3$ has $p > 0$ zero moments, then as $j \to -\infty$:*

$$|\langle \Gamma_s, \psi^k_{j,n} \rangle| \asymp 2^{j(p+1)} \rho^{-p} \text{ for } n \in \Lambda^k_j, \tag{29}$$

where $\Lambda^k_j := \{n \in \mathbb{Z}^2 \mid$ the support of $\psi^k_{j,n}$ intersects with $F\}$.

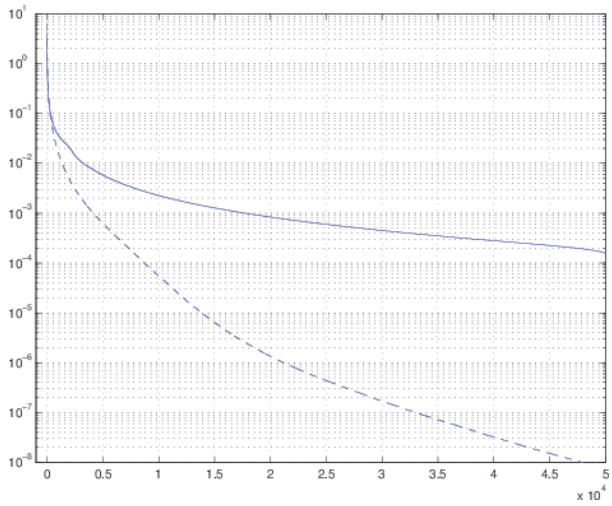

Figure 2: First 5×10^4 singular values of $\mathbf{L}$ computed with a wavelet basis. The curve with dashed and solid line correspond respectively to the far-field and the near-field measurement systems of Figure 1.

As a consequence of the stability, the data $\mathbf{V}$ of the far-field measurement reside in a low dimensional subspace while those of the near-field measurement reside in a high dimensional subspace. Therefore, the type of estimation of $\mathbf{X}$ and *afortiori* the type of basis for the implementation of estimator, should be adapted to the physical configuration of the measurement system. In the next sections, we show that in the case of the far-field measurement, the polynomial basis with linear estimation is well suited, while for the near-field measurement case it is possible to use a wavelet basis which creates a high dimensional but sparse matrix $\mathbf{X}$, and to reconstruct more information by a nonlinear estimator.

3 Polynomial basis and linear estimation

Under the homogeneous polynomial basis, the coefficients in $\mathbf{X}$ are given as follows:

$$\mathbf{X}_{\alpha\beta} := \mathcal{T}(x^\alpha, x^\beta) \tag{30}$$

with α, β being multi-indices. These $\mathbf{X}_{\alpha\beta}$ are also referred as *Generalized Polarization Tensors* (GPTs) in the perturbation theory of small inclusions [5, 7]. The coefficient vectors $\boldsymbol{\gamma}_{x_s}$ and $\boldsymbol{\gamma}_{y_r}$ in (23) are now obtained by the Taylor expansion of the Green functions:

$$V_{sr} = \sum_{|\alpha|,|\beta|=1}^{K} \frac{(-1)^{|\alpha|+|\beta|}}{\alpha!\beta!} \partial^\alpha \Gamma(x_s) \mathbf{X}_{\alpha\beta}[D] \partial^\beta \Gamma(y_r) + E_{sr}. \tag{31}$$

Moreover, the truncation error E_{sr} can be expressed explicitly, and in case of the far-field measurement it decays as $O((\delta/\rho)^{K+2})$ [2] (with δ being the size of D and $\rho > \delta$ being the radius of the measurement circle), which is far better than the previous bound (18).

Expression (31) can be simplified to the matrix product form (26) by recombining all $\mathbf{X}_{\alpha\beta}$ of order $|\alpha| = m$ and $|\beta| = n$ using coefficients of harmonic polynomials. The resulting linear operator $\mathbf{L}$ is injective for the far-field system (Figure 1 (a)) having $N_S > 2K$ transmitters, and its singular value decays as $\lambda_{mn} = O((mn)^{-1}(\delta/\rho)^{\frac{m+n}{2}})$; see [2, 3].

3.1 Linear estimator of X

Due to the global character of the polynomials, in general the coefficient matrix $\mathbf{X}$ is full. On the other hand, the fast decay of truncation error under the polynomial basis suggests that the energy of $\mathbf{X}$ is concentrated in the low order coefficients. Therefore, the simple truncation in the reconstruction order provides an effective regularization, and the first K order coefficients can be estimated by solving the least-squares problem

$$\mathbf{X}^{\text{est}} := \arg\min_{\mathbf{X}} \|\mathbf{L}(\mathbf{X}) - \mathbf{V}\|_F^2, \tag{32}$$

where $\|\cdot\|_F$ denotes the Frobenius norm. The following bound on the error of the estimation can be established: for $m, n = 1 \dots 2K$,

$$\sqrt{\mathbb{E}(((\mathbf{X}^{\text{est}})_{mn} - (\mathbf{X})_{mn})^2)} \le C \frac{\sigma_{\text{noise}}}{N_S} mn(\delta/\rho)^{-\frac{m+n}{2}}. \tag{33}$$

As a consequence, the maximum resolving order K is bounded by [2]

$$K \lesssim \log_{\delta/\rho} \sigma_{\text{noise}}. \tag{34}$$

Hence, the far-field measurement has a very limited resolution. However, the first few orders of coefficients contain important geometric information of the shape (*e.g.* the first order tells how a target resembles an equivalent ellipse), and can be used to construct shape descriptors for the identification of shapes. We refer the reader to [2] for detailed numerical results.

4 Wavelet basis and nonlinear estimation

In this section we use the wavelet (more exactly, the scaling function ϕ) introduced in section 2.3.1 for the representation $\mathcal{T}$ and the reconstruction of $\mathbf{X}$. This yields a sparse and local representation, and makes the wavelets an appropriate choice of basis for the near-field measurement which allows the reconstruction via ℓ^1 minimization and the visual perception of ∂D.

4.1 Wavelet coefficient matrix

For the wavelet basis, we use the scale number L (in place of K as in section 2.3) to denote the truncation order. The coefficient matrix $\mathbf{X} = \mathbf{X}[D, L, L]$ under the wavelet basis contains the approximation coefficients

$$\mathbf{X}_{n,n'} = \mathcal{T}(\phi_{L,n}, \phi_{L,n'}), \tag{35}$$

so that $\mathcal{T}(P_L f, P_L g) = \mathbf{f}^\top \mathbf{X} \mathbf{g}$ with P_L being the orthogonal projector onto the approximation space V_L as introduced in section 2.3.3, and $\mathbf{f}, \mathbf{g}$ are the coefficient vectors

$$\mathbf{f} = [\{\langle f, \phi_{L,n}\rangle\}_n], \ \ \mathbf{g} = [\{\langle g, \phi_{L,n}\rangle\}_n]. \tag{36}$$

The matrix $\mathbf{X}$ of a flower-shaped target is shown in Figure 3 (a).

4.2 Properties of the wavelet coefficient matrix

In the following we discuss some important properties of the wavelet coefficient matrix.

Bounds of matrix norm Proposition 4.1 establishes bounds on the spectral norm of $\mathbf{X}$ showing that $\|\mathbf{X}\|_2$ diverges as $L \to -\infty$. The proof is based on the inverse estimate and the polynomial exactness of the wavelet basis, and is given in Appendix C.

Proposition 4.1. *When $L \to -\infty$, the spectral norm of the matrix $\mathbf{X}$ is bounded by*

$$C' 2^{-L} \le \|\mathbf{X}\|_2 \le C 2^{-3L} \tag{37}$$

with $C, C' > 0$ being some constants independent of L.

Sparsity From the definition of $\mathcal{T}$ we observe that $\mathcal{T}(\phi_{j,n}, \phi_{j,n'})$ is non-zero only when the support of both wavelets intersect ∂D. Therefore, the non-zero coefficients of $\mathbf{X}$ carry geometric information on ∂D. Moreover, $\mathbf{X}$ is a sparse matrix. In fact, when the scale $L \to -\infty$ there are $\sim 2^{-2L}$ wavelets contributing to D, so the dimension of X is $\sim 2^{-4L}$. On the other hand, the number of wavelets intersecting ∂D is $\sim 2^{-L}$. Hence, the number of non zero coefficients is about 2^{-2L} and the sparsity of $\mathbf{X}$ is asymptotically 2^{2L}.

Band diagonal structure Numerical computations show that the pattern of non-zeros in $\mathbf{X}$ has a band diagonal structure. The largest coefficients appear around several principal band diagonals in a regular manner that reflects different situations of interaction between wavelets via the bilinear form $\mathcal{T}$, as shown in Figure 3 (a). We notice that the major band diagonals describe the interaction between a $\phi_{L,n}$ and its immediate neighbors (the width of the band is proportional to the size of the support of $\phi_{L,n}$). In particular, the main diagonal corresponds to the case $n = n'$, while the other band diagonals describe the interactions between other non-overlapping $\phi_{L,n}$ and $\phi_{L,n'}$.

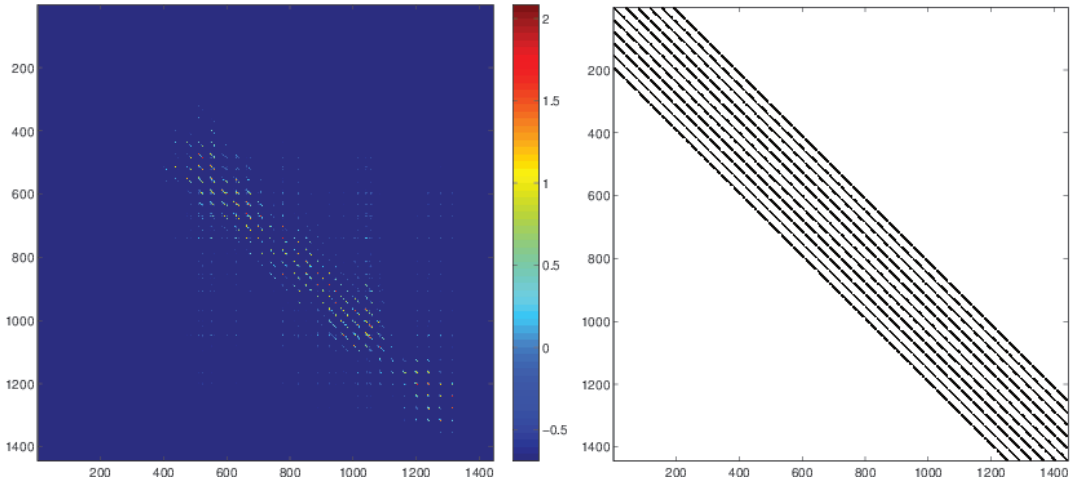

(a) $\mathbf{X}$ (b) Mask $\mathbf{M}$

Figure 3: (a): Wavelet coefficient matrix $\mathbf{X}$ of a flower-shaped target with $L = -5$ computed using Daubechies wavelet of order 6. Image is the amplitude of coefficients in logarithmic scale. Only the first 5‰ of largest coefficients (in magnitude) are shown, and the relative error of the N-term approximation is $\sim 3\%$. The number of wavelets contributing to Ω is 38×38. (b): Diagonal mask $\mathbf{M}$ for the estimation of $\mathbf{X}$ (11 band diagonals). There are $\sim 7\%$ non-zeros in $\mathbf{M}$ and the relative error of approximation of $\mathbf{X}$ with this mask is $\sim 3\%$.

Localization of ∂D Numerical evidence further suggests that the strongest coefficients appear around the major band diagonal of $\{\mathcal{T}(\phi_{L,n}, \phi_{L,n'})\}_{n,n'}$, *i.e.*, when n and n' are close. Therefore, a large value in the diagonal coefficient $\mathcal{T}(\phi_{L,n}, \phi_{L,n})$ indicates the presence of ∂D in the support of $\phi_{L,n}$. We plot the 815-th column of $\mathbf{X}$ in Figure 4, which correspond to the interaction between $\phi_{L,n}, n = [17, 21]$ and all others $\phi_{L,n'}, n' \in \mathbb{Z}^2$. We call this the *localization* property of $\mathbf{X}$. It indicates that the operator $(\lambda I - \mathcal{K}_D^*)^{-1}$ can loosely preserve the essential support of a localized $L^2(\partial D)$ function. The next proposition gives a qualitative explanation when D is the unit disk.

Proposition 4.2. *Let D be a unit disk. As $L \to -\infty$ we have*

$$|\mathcal{T}(\phi_{L,n}, \phi_{L,n'})| = \begin{cases} O(2^{-2L}) & \text{for overlapped } \phi_{L,n}, \phi_{L,n'}, \\ O(2^{-L}) & \text{otherwise.} \end{cases} \tag{38}$$

Proof. For D being a unit disk, one has [7]:

$$\mathcal{K}_D^*[f](x) = \frac{1}{4\pi}\int_{\partial D} f(y)ds(y).$$

By simple manipulations one can deduce that

$$(\lambda I - \mathcal{K}_D^*)^{-1}[f](x) = \lambda^{-1}(I + (\kappa-1)\mathcal{K}_D^*)(f)(x). \tag{39}$$

Therefore, the bilinear form $\mathcal{T}(f,g)$ is reduced to

$$\int_{\partial D} g(\lambda I - \mathcal{K}_D^*)^{-1}\left[\frac{\partial f}{\partial \nu}\right]ds = \frac{1}{\lambda}\int_{\partial D} g\frac{\partial f}{\partial \nu}ds + \frac{\kappa-1}{4\pi\lambda}\int_{\partial D} g\,ds\int_{\partial D}\frac{\partial f}{\partial \nu}ds. \tag{40}$$

Taking $f = \phi_{L,n}$ and $g = \phi_{L,n'}$ as $L \to -\infty$ the intersection between ∂D and the support of $\phi_{L,n}$ is well approximated by a line segment. By a change of variables, it follows that

$$\int_{\partial D}\phi_{L,n'}ds\int_{\partial D}\partial_\nu\phi_{L,n}ds = O(2^{-L}). \tag{41}$$

Similarly, one has

$$\int_{\partial D}\phi_{L,n'}\partial_\nu\phi_{L,n}ds = \begin{cases} O(2^{-2L}) & \text{for overlapped } \phi_{L,n}, \phi_{L,n'}, \\ 0 & \text{otherwise.} \end{cases} \tag{42}$$

Substituting (41) and (42) into (40) yields (38). □

Hence, as $L \to -\infty$, the coefficients of the main diagonal behave like $O(2^{-2L})$, and dominate the other band diagonals that behave like $O(2^{-L})$.

4.3 Wavelet based imaging algorithms

The localization property of $\mathbf{X}$ can be used to visualize the target D. A simple algorithm, called *imaging by diagonal*, consists in taking the diagonal of $\mathbf{X}$ (*i.e.*, the coefficients $\mathcal{T}(\phi_{L,n},\phi_{L,n})$) and reshaping it to a 2D image. Then the boundary of ∂D can be read off from the image.

A drawback of this method is that the generated boundary has low resolution. In fact, any $\phi_{L,n}$ touching the boundary ∂D is susceptible to yield a numerically non-negligible value of $\mathcal{T}(\phi_{L,n},\phi_{L,n})$. Hence, larger is the support of the wavelet, more are the wavelets intersecting ∂D and lower is the resolution. An improved method consists in searching for each index $n \in \mathbb{Z}^2$, the index n' maximizing the interaction between $\phi_{L,n}, \phi_{L,n'}$:

$$n' = \arg\max_{n'\in\mathbb{Z}^2}|\mathcal{T}(\phi_{L,n},\phi_{L,n'})|, \tag{43}$$

and then accumulating $|\mathcal{T}(\phi_{L,n},\phi_{L,n'})|$ for the index n. We name this method *imaging by maximum*. It is higher in resolution since the effect of the wavelets touching merely ∂D is absorbed by their closest neighbors lying on ∂D. The procedure is summarized in Algorithm 1. Figures 5 (a) and (b) show a comparison between these two algorithms.

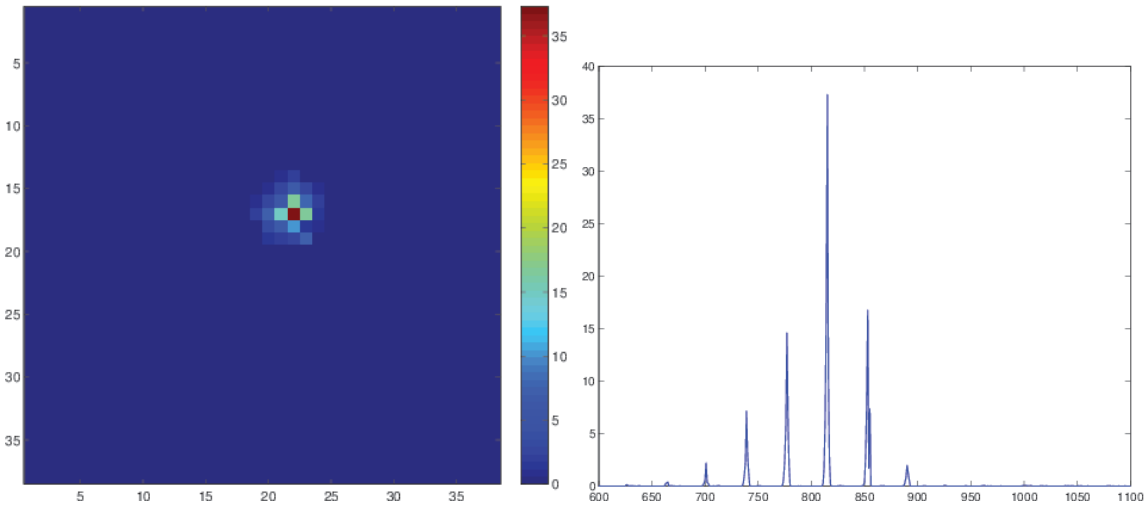

(a) (b)

Figure 4: Amplitude of $\{\mathcal{T}(\phi_{L,n}, \phi_{L,n'})\}_{n'}$ with $L = -4, n = [17, 21]$ (or equivalently the 815-th row in Figure 3 (a)). The support of the wavelet $\phi_{L,n}$ intersects ∂D. (a): View as an image with each pixel corresponding to one n'. (b): Amplitude as a function of the position index n'. The highest peak appears around $n' = 815$.

Algorithm 1 Imaging by maximum

Input: the matrix $\mathbf{X}$ of an unknown shape D, a zero-valued matrix I.

for $n \in \mathbb{Z}^2$ **do**

1. $n' \leftarrow \arg\max_{n' \in \mathbb{Z}^2} |\mathbf{X}_{n,n'}|$
2. $I(n) \leftarrow I(n) + |\mathbf{X}_{n,n'}|$;

end for

Output: the 2D image I.

4.4 Reconstruction of X by ℓ^1 minimization

As the scale L decreases, the dimension of $\mathbf{X}$ increases rapidly as $\propto 2^{-4L}$. On the other hand, the band diagonal structure of $\mathbf{X}$ shows that the largest coefficients distribute on the major band diagonals, which is an important *a priori* information allowing to reduce considerably the dimension of the unknown to be reconstructed.

For this, we fix *a priori* $N_0 > 0$ and assume that the coefficient $\mathcal{T}(\phi_{L,n}, \phi_{L,n'})$ can be neglected when $|n - n'| > N_0$. We construct accordingly a band diagonal mask $\mathbf{M}$ taking values 0 or 1 by choosing N_0 proportional to the support size of the wavelet. Remark that the mask constructed in this way is not adaptive and does not contain any information about the boundary of the target. Figure 3 (b) shows a mask $\mathbf{M}$ with $N_0 = 5$.

Given the high dimension of $\mathbf{X}$ and its sparsity, we seek a sparse solution by solving the

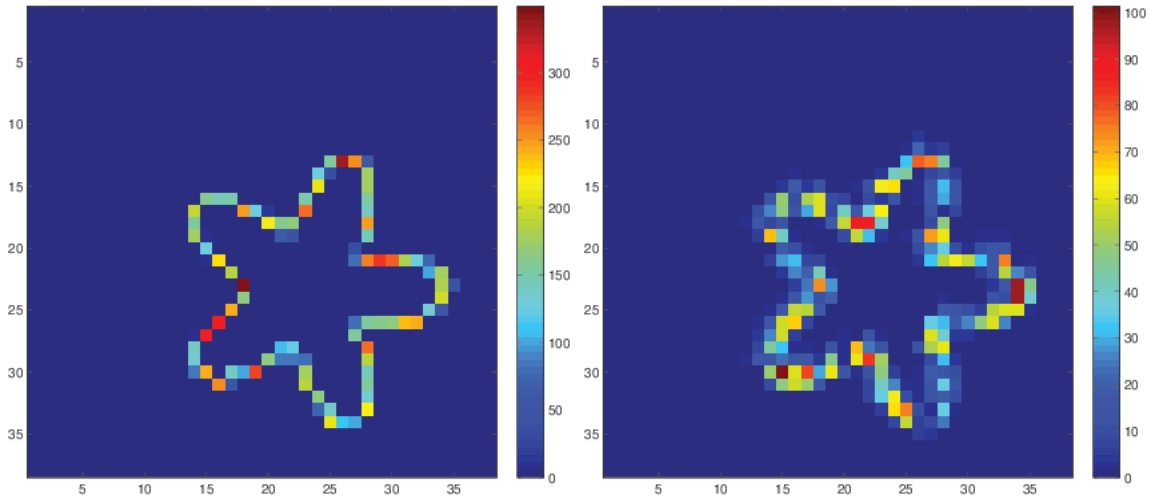

(a) (b)

Figure 5: Images obtained by the imaging algorithms 4.3 applied on the true coefficients $\mathbf{X}$ with $L = -4$. (a): Imaging by maximum. (b): Imaging by diagonal.

ℓ^1 minimization problem as follows [19, 13, 10]:

$$\mathbf{X}^{\text{est}} := \arg\min_{\mathbf{X}} \|\mathbf{L}(\mathbf{M} \odot \mathbf{X}) - \mathbf{V}\|^2 + \mu \|\mathbf{M} \odot \mathbf{X}\|_{1,w}, \tag{44}$$

where $\mathbf{M}$ is the band diagonal mask (Figure 3 (b)), $\odot$ denotes the termwise multiplication, $\mu > 0$ is the regularization parameter, and $\|\mathbf{x}\|_{1,w} = \sum_n w_n |x_n|$ is the reweighted ℓ_1 norm. We set the weight w in such a way that the operator $\mathbf{L}$ is normalized columnwisely. The constant μ is determined by the universal threshold [19] (tuned manually to achieve the best result if necessary):

$$\mu \propto \sigma_{\text{noise}} \sqrt{N_s N_r} \sqrt{2 \log \|\mathbf{M}\|_1} \tag{45}$$

with $\|\mathbf{M}\|_1$ being the number of non-zero values in $\mathbf{M}$. Problem (44) admits a unique sparse solution [19] under appropriate conditions, and can be solved numerically via efficient algorithms; see for example [8].

5 Numerical experiments

In this section we present some numerical results to illustrate the efficiency of the wavelet imaging algorithm proposed in section 4.3. The wavelet used here is the Daubechies wavelet of order 6. We consider a near-field measurement system (Figure 1 (b)) with 20×20 uniformly distributed sources and receivers.

5.1 Parameter settings

We set the conductivity constant $\kappa = 4/3$ and use a flower-shaped target as D. The whole procedure of the experiment is as follows. First, the data V_{sr} are simulated by evaluating

(8) for all sources x_s and receivers y_r of the measurement system. A white noise of level

$$\sigma_{\text{noise}} = \sigma_0 \|\mathbf{V}\|_F / \sqrt{N_s N_r} \tag{46}$$

is added to obtain the noisy data $\mathbf{V}$, with σ_0 being the percentage of noise in data. Thereafter the minimization problem (44) is solved with the parameters and methods described in section 4.4. Finally, from the reconstructed coefficients $\mathbf{X}$, we apply Algorithm 1 to obtain a pixelized image of ∂D.

The vectors $\boldsymbol{\gamma}_{x_s}, \boldsymbol{\gamma}_{y_r}$ in (23) contain the wavelet coefficients of the Green functions Γ_s and Γ_r respectively. They are computed by first sampling Γ_s and Γ_r on a fine Cartesian lattice of sampling step $\lesssim 2^{-11}$ on Ω (the singularity point x_s is numerically smoothed) and then applying the discrete fast wavelet transform on these samples to obtain the coefficients at the desired scale.

5.2 Results of the imaging algorithm

Figures 6 (a, b) show the results of imaging obtained at the scale $L = -4$ with different noise levels. It can be seen that even in a highly noisy environment (*e.g.* $\sigma_0 = 100\%$) the boundary of D can still be correctly located.

Remark that for the near-field internal measurement system Figure 1 (b), one can obtain an image of ∂D directly from the data $\mathbf{V}$ (in fact, V_{sr} being defined by (8) has large amplitude if x_s and/or y_r is close to ∂D). Nonetheless, such a direct imaging method is far less robust to noise than the wavelet based algorithm and its resolution is limited by the density of the transmitters, as shown in Figures 6 (c, d).

In Figure 7 the same experiments of imaging with noisy data were conducted at the scale $L = -5$. We notice that the images returned by Algorithm 1 have dimension 64×64, which is much higher than that of the grid of transmitters (20×20). Furthermore, the results remain robust up to the noise level $\sigma_0 = 50\%$. These confirm the super-resolution character of the wavelet based imaging algorithm.

6 Discussion

6.1 Effect of the conductivity constant κ

The constant κ as defined in section 2 is actually the ratio between the conductivity of the target and the background (set to 1 in this paper). Further numerical experiments suggest that the performance of Algorithm 1 depend on κ: the results may deteriorate when κ becomes large (*e.g.* $\kappa \geq 4$). This can be explained easily for the case of a unit disk. In fact, it can be seen from (40) that the ratio between the overlapped and non overlapped (in terms of the functions $\phi_{L,n}, \phi_{L,n'}$) coefficients of $\mathbf{X}$ varies with κ as $1/(\kappa - 1)$. Hence, the localization property (section 4.2) becomes more (resp. less) pronounced when $\kappa \to 1$ (resp. $\kappa \to +\infty$), and the imaging algorithm is impacted accordingly. Nonetheless, we note also that when $\kappa \to 1$, the target D becomes indistinguishable from the background and the measured data $\mathbf{V}$ decreases to zero (without considering the noise). These observations suggest that in practice there may exist some numerical ranges for κ and for the noise level on which the imaging algorithm is more or less effective.

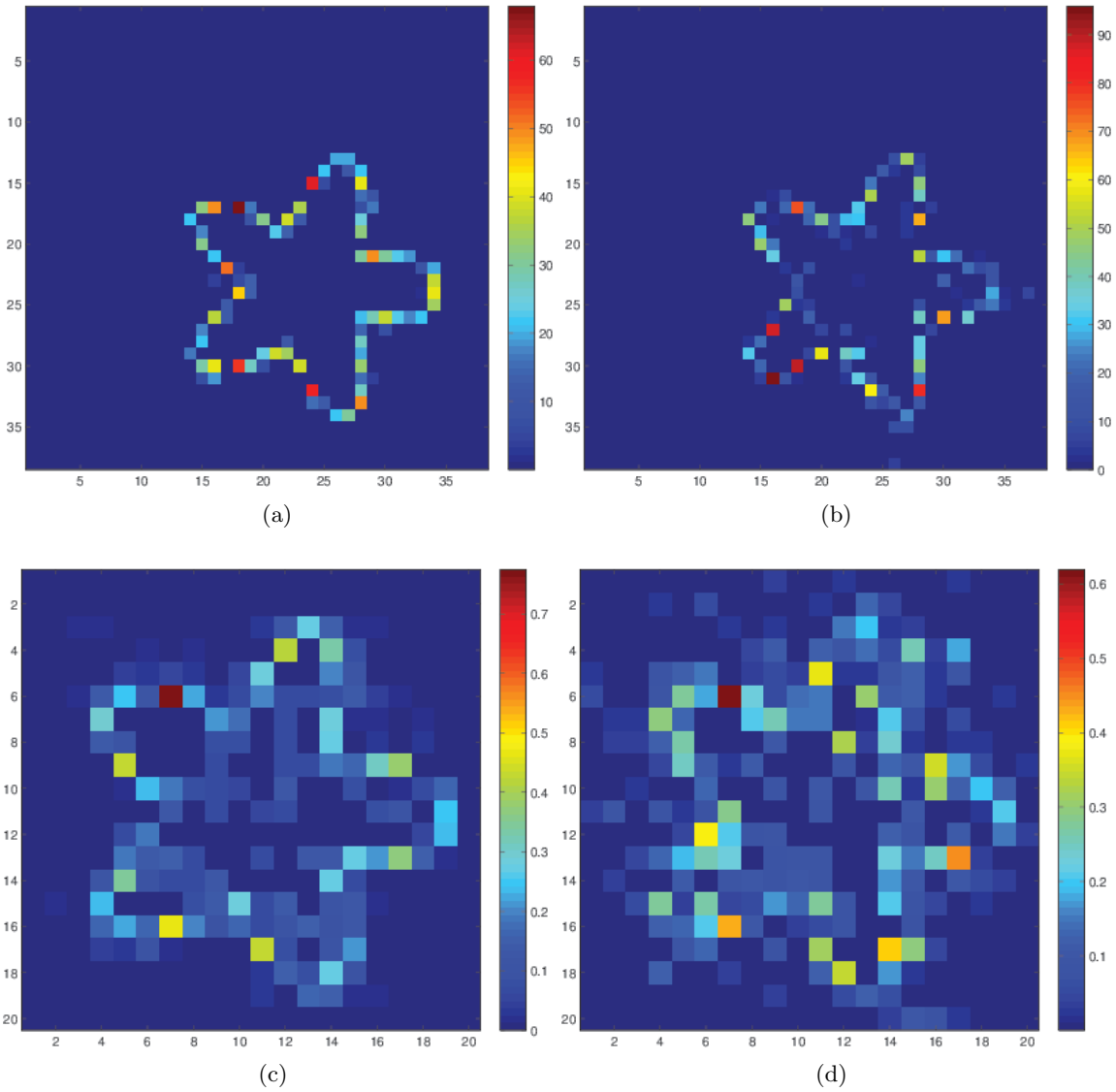

Figure 6: (a, b): Images obtained by Algorithm 1 applied on $\mathbf{X}$ reconstructed from data with noise, $L = -4$. (c, d): Images obtained directly from data $\mathbf{V}$. (a, c): Noise level $\sigma_0 = 50\%$, (b, d): $\sigma_0 = 100\%$.

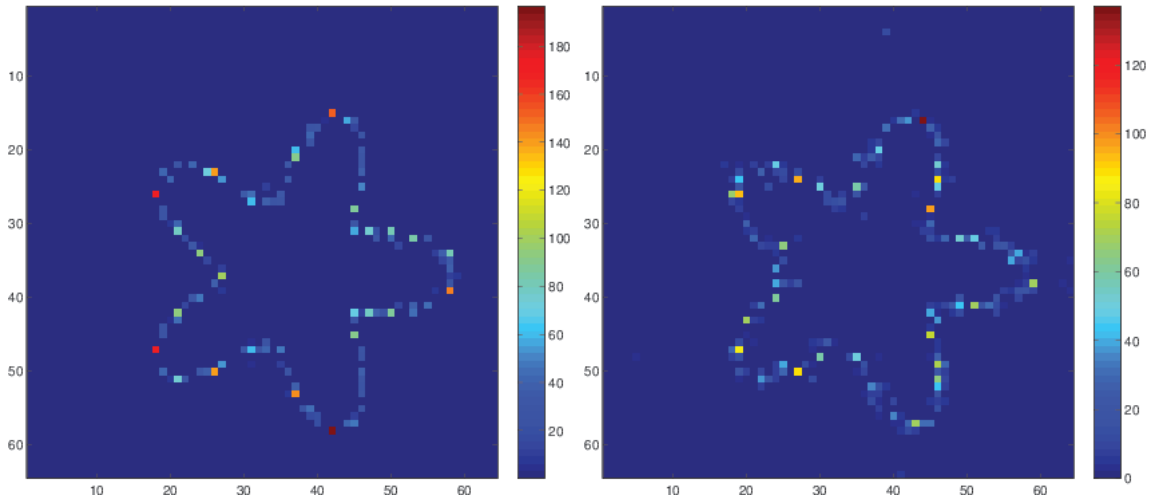

(a) (b)

Figure 7: Same experiments as Figures 6 (a, b) at the scale $L = -5$. (a): Imaging by maximum with $\sigma_0 = 10\%$ of noise, (b): with $\sigma_0 = 50\%$ of noise.

6.2 Representation with the wavelet ψ

In section 4 we used only the scaling function ϕ for the approximation and the representation of $\mathcal{T}$, while it is also possible to use the wavelet functions ψ^k together with ϕ to represent $\mathcal{T}$ and obtain another form of $\mathbf{X}$. More precisely, let W_j be the detail space spanned by $\{\psi^k_{j,n}\}_{n\in\mathbb{Z}^2,k=1,2,3}$ and Q_j be the orthogonal projectors onto W_j. For any two scales $L \leq J$, it holds

$$\begin{aligned}\mathcal{T}(P_L f, P_L g) = &\sum_{j,j'=L+1}^{J} \underbrace{\mathcal{T}(Q_j f, Q_{j'} g)}_{D_{j,j'}} + \sum_{j'=L+1}^{J} \underbrace{\mathcal{T}(P_J f, Q_{j'} g)}_{C_{J,j'}} \\ &+ \sum_{j=L+1}^{J} \underbrace{\mathcal{T}(Q_j f, P_J g)}_{B_{j,J}} + \underbrace{\mathcal{T}(P_J f, P_J g)}_{A_{J,J}} = \mathbf{f}^\top \mathbf{X} \mathbf{g}, \end{aligned} \tag{47}$$

where we used the fact that $P_L f = P_J f + \sum_{j=L+1}^{J} Q_j f$, and $\mathbf{f}, \mathbf{g}$ are respectively the coefficient vectors of f and g under the basis $\{\phi_{J,n}, n \in \mathbb{Z}^2\} \cup \{\psi^k_{j,n}, j = L \dots J, n \in \mathbb{Z}^2, k = 1, 2, 3\}$. The coefficient matrix $\mathbf{X}$ now takes the form

$$\mathbf{X} = \mathbf{X}[D, L, J] = \begin{pmatrix} D_{L+1,L+1} & \dots & D_{L+1,J} & B_{L+1,J} \\ \vdots & \ddots & \vdots & \vdots \\ D_{J,L+1} & \dots & D_{J,J} & B_{J,J} \\ C_{J,L+1} & \dots & C_{J,J} & A_{J,J} \end{pmatrix}, \tag{48}$$

where D, C, B, and A denote the block matrices corresponding to the terms marked by braces in (47) respectively. In particular, $D_{j,j'}$ contains the detail coefficients of type

$\mathcal{T}(\psi^k_{j,n}, \psi^{k'}_{j',n'})$ with $k, k' = 1, 2, 3$, while $A_{J,J}$ contains the approximation coefficients $\mathcal{T}(\phi_{J,n}, \phi_{J,n'})$. Remark that in the case $L = J$, $\mathbf{X}[D, L, L]$ is reduced to $A_{L,L}$ which is identical to the coefficient matrix defined in (35).

Moreover, one can easily prove (using the conjugated filters) that for any $J, J' \geq L$, $\mathbf{X}[D, L, J']$ and $\mathbf{X}[D, L, J']$, regarded as $\ell^2(\mathbb{Z})$ vectors, are equivalent up to an ℓ^2 unitary transform. Therefore the choice of the scale J is not important since $\mathbf{X}[D, L, J]$ is equivalent to $\mathbf{X}[D, L, L]$ for any $J \geq L$, and their dimensions are asymptotically equal as $L \to -\infty$ for a fixed domain Ω.

A natural question is to know whether the equivalent representation $\mathbf{X}[D, L, J]$ with $J < L$ is more sparse than $\mathbf{X}[D, L, L]$. In Figure 8 we plot the decay of the coefficients of the four block matrices in $\mathbf{X}[D, L, L+1]$ with $L = -5$. It can be seen that for the numerical range considered here, the detail coefficients have similar decay as the approximation coefficients. In fact, like $\mathcal{T}(\phi_{L,n}, \phi_{L,n'})$, the main reason for the sparsity of the detail coefficients $\mathcal{T}(\psi^k_{j,n}, \psi^{k'}_{j',n'})$ is the intersection between the support of wavelets and the boundary ∂D, and for the same reason the localization property (*i.e.*, Proposition 4.2) remains valid for the wavelets $\psi^k_{j,n}, k = 1, 2, 3$. Hence the representation $\mathbf{X}[D, L, J]$ has a similar sparsity as $\mathbf{X}[D, L, L]$ and does not present substantial advantages for the applications considered in this paper.

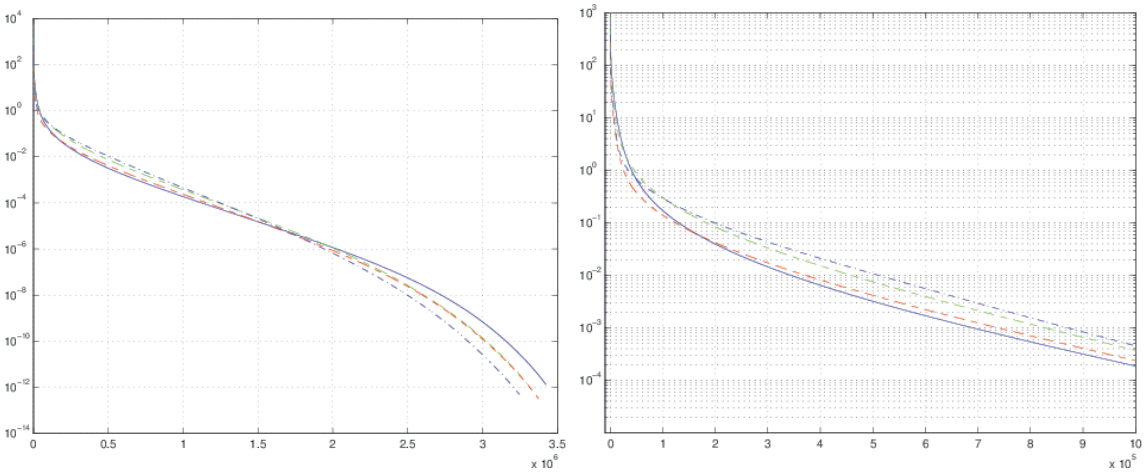

(a) (b)

Figure 8: Coefficients (absolute value) of $\mathbf{X}[D, L, L+1]$ with $L = -5$ in decreasing order in the logarithmic scale. (a): All coefficients. (b): Zoom-in on the first 10^6 coefficients. The different curves in the figures represent: $\mathcal{T}(\phi_{L,n}, \phi_{L,n'})$ (dash-dot line), $\mathcal{T}(\psi^3_{L,n}, \phi_{L,n'})$ (dashed line in green), $\mathcal{T}(\phi_{L,n}, \psi^3_{L,n'})$ (dashed line in red), and $\mathcal{T}(\psi^3_{L,n}, \psi^3_{L,n'})$ (solid line).

7 Conclusion

In this paper we presented a general framework for the electro-sensing problem, and proposed a new wavelet based approach for the solution of the inverse problem and the vi-

sualization of the target. The new approach is complementary to the previous developed polynomial based approach in that both of them can be seen as choosing the basis adapted to the measurement system. In case of the near-field measurement, the wavelet approach is more appropriate than to the polynomial approach since it gives a sparse representation of the geometric information of the target and allows to reconstruct more information by exploiting the sparsity using ℓ^1 minimization, which is superior in robustness than the linear estimator in this case. Finally, numerical results show the performance of the wavelet imaging algorithms, confirming the efficiency of the new approach.

A Proof of Lemma 2.2

Proof. For a given $g \in H^s(\Omega)$, by density of $\mathcal{C}^\infty(\Omega)$ in $H^s(\Omega)$, for any $\epsilon > 0$ there exists $u \in \mathcal{C}^\infty(\Omega)$, such that $\|g-u\|_{H^s} \leq \epsilon/2$. On the other hand, since Ω is bounded, one can construct the Bernstein polynomial to approximate a $\mathcal{C}^\infty$-function and its first s order derivatives simultaneously and uniformly on Ω [16]. Hence, there exists $K = K(\epsilon) > 0$ and a polynomial

$$p(x) = \sum_{|\alpha|_\infty \leq K} a_\alpha x^\alpha, \ x \in \mathbb{R}^2, \tag{49}$$

such that $\|u-p\|_{H^s} \leq \epsilon/2$. Therefore,

$$\|g-p\|_{H^s} \leq \|g-u\|_{H^s} + \|u-p\|_{H^s} \leq \epsilon,$$

which proves that the polynomial basis is complete in $H^s(\Omega)$ for $s \geq 0$. □

B Proof of Proposition 2.4

Proof. Since $x_s \notin F$, there exists a scale j_0 small enough such that $x_s \neq 2^j n$ for any $n \in \Lambda_j^k, j \leq j_0, k = 1,2,3$. The Taylor expansion up to order $p-1$ of Γ_s reads:

$$\Gamma_s(x) = \sum_{|\alpha|=0}^{p-1} \frac{(x-2^j n)^\alpha}{\alpha!} \partial^\alpha \Gamma(2^j n - x_s) + R(x)$$

with the rest $R(x)$ being given by

$$R(x) = \sum_{|\alpha|=p} \frac{p}{\alpha!} (x-2^j n)^\alpha \int_0^1 (1-t)^{p-1} . \partial^\alpha \Gamma(2^j n - x_s + t(x-2^j n)) dt$$

For $k = 1,2,3$, the two-dimensional wavelet $\psi_{j,n}^k$ is orthogonal to the polynomial x^α for any $|\alpha| < p$. Hence by the change of variables $x \to 2^j x$ we obtain

$$\langle \Gamma_s, \psi_{j,n}^k \rangle = \sum_{|\alpha|=p} \frac{2^{j(p+1)} p}{\alpha!} \int_0^1 (1-t)^{p-1} \int_{\operatorname{supp} \psi^k} x^\alpha \psi^k(x) \partial^\alpha \Gamma(2^j n - x_s + t 2^j x) dx \, dt. \tag{50}$$

When $j \to -\infty$, there exists positive constants c_0 and c_1 depending only on F and ψ^k, such that for any $n \in \Lambda_j^k$, the distance between x_s and $2^j n$ satisfies

$$c_0 \rho \leq \|2^j n - x_s\| \leq c_1 \rho.$$

Combining the fact that ψ^k is compactly supported together with the estimate $|\partial^\alpha \Gamma(x)| \asymp \|x\|^{-|\alpha|}$, we conclude from (50) that

$$|\langle \Gamma_s, \psi_{j,n}^k \rangle| \asymp 2^{j(p+1)} \rho^{-p} \quad \text{as } j \to -\infty,$$

where the underlying constants depend only on x_s, F, ψ^k, and p. □

C Proof of Proposition 4.1

Proof. For any $f \in H^2, g \in H^1$, let $\mathbf{f}, \mathbf{g}$ be the coefficient vectors defined in (36). By the boundness of $\mathcal{T}$, we have

$$|\mathbf{f}^\top \mathbf{X} \mathbf{g}| = |\mathcal{T}(P_L f, P_L g)| \leq C \|P_L f\|_{H^2} \|P_L g\|_{H^1}.$$

Since the scaling function $\phi \in \mathcal{C}_0^r(\mathbb{R})$ with $r \geq 2$, we have the inverse estimate ([14, Theorem 3.4.1]):

$$\|P_L f\|_{H^2} \leq C 2^{-2L} \|P_L f\|_{L^2} = C 2^{-2L} \|\mathbf{f}\|_2, \tag{51}$$

where the last identity comes from $\|P_L f\|_{L^2} = \|\mathbf{f}\|_{\ell^2}$ ($\{\phi_{L,n}\}_{n \in \mathbb{Z}^2}$ is an orthonormal basis of the approximation space V_L). Similarly, one has the inverse estimate $\|P_L g\|_{H^1} \leq C 2^{-L} \|\mathbf{g}\|_2$. Finally, we obtain

$$|\mathbf{f}^\top \mathbf{X} \mathbf{g}| \leq C 2^{-3L} \|\mathbf{f}\|_{\ell^2} \|\mathbf{g}\|_{\ell^2},$$

which proves the right-hand side of (37).

Let D_ϵ be a circular domain of width ϵ around ∂D defined as

$$D_\epsilon = \{x \,|\, \operatorname{dist}(x, \partial D) \leq \epsilon\}. \tag{52}$$

Let $\eta > \epsilon$ and D_η be another circular domain containing D_ϵ, and put

$$f(x) = \begin{cases} x_1 & \text{if } x \in D_\eta, \\ 0 & \text{otherwis.} \end{cases}$$

As $L \to -\infty$ we can choose the constant $\eta \propto 2^L$ such that any $\phi_{L,n}$ whose support intersects D_ϵ has its support strictly included in D_η. Now by definition of the wavelet basis $\mathcal{B}$ in section 2.3.3, the approximation space V_L contains polynomials of order $p-1$. Therefore, when restricted on D_ϵ,

$$f|_{D_\epsilon} = (P_L f)|_{D_\epsilon}. \tag{53}$$

On the other hand, explicit bounds exist on the generalized polarisation tensors (30) $\mathbf{X}_{\alpha,\beta}$ ([7, Lemma 4.12]). In particular, for $|\alpha| = 1$ the following estimate holds [12]

$$|D| \leq \frac{\kappa+1}{|\kappa-1|}\,|\mathcal{T}(x^\alpha, x^\alpha)| \leq C|D| \tag{54}$$

with C being some constant independent of D and $|D|$ being the volume of D. Hence, if $\mathbf{f}$ is the coefficient vector of $P_L f$, using (53) we obtain that

$$|\mathbf{f}^\top \mathbf{X}\mathbf{f}| = |\mathcal{T}(P_L f, P_L f)| = |\mathcal{T}(f,f)| = |\mathcal{T}(x_1,x_1)| \geq \frac{|\kappa-1|}{\kappa+1}|D|.$$

Finally, notice that $\|\mathbf{f}\|^2_{\ell^2} = \|P_L f\|^2_{L^2} \leq \|f\|^2_{L^2} \lesssim 2^L$, which gives the left-hand side of (37). □

References

[1] H. Ammari, T. Boulier, and J. Garnier. Modeling active electrolocation in weakly electric fish. *SIAM J. Imag. Sci.*, 5:285–321, 2013. 8

[2] H. Ammari, T. Boulier, J. Garnier, W. Jing, H. Kang, and H. Wang. Target identification using dictionary matching of generalized polarization tensors. *Found. Comp. Math., DOI 10.1007/s10208-013-9168-6*, 2013. 1, 2, 9, 10

[3] H. Ammari, T. Boulier, J. Garnier, H. Kang, and H. Wang. Tracking of a mobile target using generalized polarization tensors. *SIAM J. Imag. Sci.*, 6:1477–1498, 2013. 9, 10

[4] H. Ammari, T. Boulier, J. Garnier, and H. Wang. Shape recognition and classification in electro-sensing. *arXiv:1302.6384*, 2013. 8

[5] H. Ammari, J. Garnier, W. Jing, H. Kang, M. Lim, K. Solna, and H. Wang. *Mathematical and Statistical Methods for Multistatic Imaging*. Springer Verlag, 2013. 2, 10

[6] H. Ammari, J. Garnier, H. Kang, M. Lim, and S. Yu. Generalized polarization tensors for shape description. *Numer. Math., DOI 10.1007/s00211-013-0561-5*, 2013. 9

[7] H. Ammari and H. Kang. *Polarization and Moment Tensors: With Applications to Inverse Problems and Effective Medium Theory*, volume 162. Springer Verlag, 2007. 3, 10, 13, 22

[8] A. Beck and M. Teboulle. A fast iterative shrinkage-thresholding algorithm for linear inverse problems. *SIAM J. Imag. Sci.*, 2(1):183202, 2009. 15

[9] L. Borcea. Electrical impedance tomography. *Inverse problems*, 18(6):99136, 2002. 1

[10] E. J. Candes and T. Tao. Near-optimal signal recovery from random projections: Universal encoding strategies? *Information Theory, IEEE Transactions on*, 52(12):54065425, 2006. 15

[11] C. Canuto and A. Quarteroni. Approximation results for orthogonal polynomials in sobolev spaces. *Math. Comp.*, 38(157):6786, 1982. 5

[12] Y. Capdeboscq and M. S. Vogelius. Optimal asymptotic estimates for the volume of internal inhomogeneities in terms of multiple boundary measurements. *M2AN Math. Model. Numer. Anal.*, 37(2):227–240, 2003. 22

[13] S. S. Chen, D. L. Donoho, and M. A. Saunders. Atomic decomposition by basis pursuit. *SIAM J. Sci. Comp.*, 20(1):33–61, January 1998. 15

[14] A. Cohen. *Numerical Analysis of Wavelet Methods*, volume 32. JAI Press, 2003. 6, 21

[15] A. Cohen and I. Daubechies. A new technique to estimate the regularity of refinable functions. *Revista matemtica iberoamericana*, 12(2):527–591, 1996. 5

[16] E. H. Kingsley. Bernstein polynomials for functions of two variables of class c(k). *Proc. Amer. Math. Soc.*, 2(1):64–71, 1951. 20

[17] O. Kwon, J. K. Seo, and J. R Yoon. A real time algorithm for the location search of discontinuous conductivities with one measurement. *Comm. Pure Appl. Math.*, 55(1):1–29, 2002. 2

[18] E. Lee, J. K. Seo, E. J. Woo, and T. Zhang. Mathematical framework for a new microscopic electrical impedance tomography system. *Inverse Problems*, 27:p. 055008, 2011. 8

[19] S. Mallat. *A Wavelet Tour of Signal Processing: the Sparse Way*. Academic press, 2008. 5, 6, 15

[20] M. S. Mannoor, S. Zhang, A. J. Link, and M. C. McAlpine. Electrical detection of pathogenic bacteria via immobilized antimicrobial peptides. *Proc. Nat. Acad. Sci., USA*, 107:19207–19212, 2010. 8

[21] Y. Meyer and D. H. Salinger. *Wavelets and Operators*, volume 37. Cambridge Univ Press, 1992. 6